

Research Article

Investigating the Macro-Micromechanical Properties and Failure Law of Granite under Loading and Unloading Conditions

Chao Peng ^{1,2} Jianbo Wang,^{1,2} Huanxin Liu ^{1,2,3} Guilin Li,^{1,2} and Wei Zhao⁴

¹Deep Mining Laboratory of Shandong Gold Group Co., Ltd., Laizhou 261442, China

²Shandong Key Laboratory of Deep-sea and Deep-earth Metallic Mineral Intelligent Mining, Laizhou 261442, China

³School of Civil and Resource Engineering, University of Science and Technology Beijing, Beijing 100083, China

⁴Shandong Gold Group Yantai Design and Research Engineering Co., Ltd. Yantai 261442, China

Correspondence should be addressed to Huanxin Liu; ssdxmb@163.com

Received 5 March 2021; Revised 29 June 2021; Accepted 28 July 2021; Published 3 August 2021

Academic Editor: Xun Xi

Copyright © 2021 Chao Peng et al. This is an open access article distributed under the Creative Commons Attribution License, which permits unrestricted use, distribution, and reproduction in any medium, provided the original work is properly cited.

The excavation of rock significantly changes the initial stress state of rock slopes, which makes rock in complex loading and unloading conditions. However, the failure mechanisms and macro-micromechanical properties of rock under loading and unloading conditions are not very clear. This study investigates the macro-micromechanical properties and failure law of granite under loading and unloading conditions through traditional laboratory tests and particle flow simulations. Granite specimens are taken from Shuichang iron mine, and stress unloading experiments are designed based on the engineering practices. The stress-strain curves and failure modes under different confining pressures and unloading paths are obtained to analyze the granite properties from the viewpoint of the macroscopic mechanism. Moreover, numerical models are established in PFC software. The microcracks developments, failure characteristics, and energy evolutions under loading and unloading conditions are obtained and discussed. Results show that compared with the loading tests, the brittle failure characteristics of specimens under unloading tests are more obvious. When the confining pressure reduces to about 66% of the initial confining pressure, the specimen loses its load-bearing capacity and destroyed due to the lateral expansion. For loading tests, an inclined plane can be produced as the main failure surface. While for confining pressure unloading tests, there are many damage zones parallel to or intersecting with the main failure surface.

1. Introduction

Rock excavation will significantly change the stress state of rock mass, which affects the stability and performance of rock engineering (e.g., open-pit slope, shaft, tunnels, wells, and stopes) [1]. The redistributed stress of rock after excavation can be in loading or unloading states. For examples, when the rock is excavated in a circular tunnel, rock around the tunnel surface will be in an unloading state at the radial direction, while in a loading state at the hoop direction. Moreover, the loading and unloading are two completely different stress paths, resulting in different mechanical responses [2–4]. Therefore, it is necessary to investigate the mechanical behavior and failure of rock under loading and unloading conditions.

Due to the research of rock mechanics has yielded fruitful results in loading conditions, more and more scholars begin to explore the unloading rock mechanics from various aspects such as the failure mechanism, stress-strain curve, and strength criterion. Based on the concept of Griffith microcrack in rock fracture mechanics, Lajta et al. [5] proved that unloading could lead to the formation of cracks, and the tensile failure was related to residual stress. Lau et al. [6] carried out a series of loading and unloading tests and found that the mechanical parameters obtained from unloading tests were more practical. Some scholars [7, 8] believed that the mechanical parameters obtained through the unloading path were more consistent with the actual rock excavation conditions. Shen et al. and Xi et al. [9–11] investigated the loading and unloading failure

mechanism of rock by using the stress-strain curves under different confining pressures and stress paths based on fracture mechanics of rock mass. Zhao et al. [12] and Wu et al. [13] proposed constitutive models which can describe the damage degree of rock mass under unloading conditions according to the theory of damage mechanics. Furthermore, Ajmi et al. [14] and Li et al. [15–17] analyzed the failure mechanism and the damage degradation effect of rock mechanical parameters under different paths. The results showed that the Mogi–Coulomb strength criterion was in good agreement with the experimental data. Huang et al. [18, 19] studied the mechanical characteristics of granite unloading failure under different initial confining pressures from various aspects such as deformation, parameters, and fracture characteristics, obtaining the evolution of the deformation, brittle failure, and energy under unloading conditions. Fan et al. [20] investigated the energy release process of high energy storage rock mass induced by transient unloading of in situ stress by using the local energy release rate and energy release coefficient. Liu et al. and others [21–23] studied the influence of the initial unloading level on the mechanical characteristics of rock unloading. The results showed that the initial unloading level was a dominating factor for the mechanical characteristics of rock, which had a great influence on the parameters such as force, internal friction angle, lateral strain, and maximum dilatancy. Nuclear magnetic resonance (NMR) [24], computed tomography (CT) imaging technology [25, 26], and scanning electron microscope (SEM) [27] were used to study the whole process of the microcrack growth, propagation, penetration, and failure of rock sample in unloading conditions.

Computational simulation of rock fractures has always been an active research field, which has promoted the understanding of macro-micro-mechanical properties and failure mechanism of rock [28]. PFC can overcome the limitations of continuous medium simulation software and well explain the mechanical behavior of various aspects of rock [29–31]. Cai et al. [32, 33] discussed the failure mechanism of jointed rock in underground engineering based on the peak strength and residual strength of rock obtained by PFC simulation. An et al. [34] established a dynamic simulation contact model of the rock impact test based on the discrete element method, which could better demonstrate the distribution of velocity and kinetic energy of rocks such as rock movement and rock failure under impact load. Some researchers [35–39] established an equivalent rock mass model, which could reflect the microfracture effect. They found that the equivalent rock mass technology can replace the laboratory tests or in situ tests to a certain degree. Tang et al. and others [40–45] simulated and investigated the mechanism of initiation, propagation, and coalescence of rock cracks by using PFC software.

At present, the research of rock mechanical properties, especially in unloading conditions, is mainly based on the qualitative analysis of macroscopic experimental

phenomena. In addition, due to the limitation of experimental conditions and theoretical methods, there are few research studies on micromechanical properties and failure law.

This study attempts to discuss the macro-micro-mechanical properties and failure mechanism of granite under loading and unloading conditions by laboratory tests and numerical tests. Through triaxial compression tests with constant axial stress-unloading confining pressures, the stress-strain curves of granite under different stress paths are obtained, and its macromechanical properties are studied. Using PFC3D software as the numerical analysis platform, triaxial loading and unloading simulations are carried out to study the micromechanical behavior of rock. The failure mechanism is revealed by analyzing the evolution law of microcrack and failure mode of microcrack under loading and unloading conditions.

2. Experimental Procedures

2.1. Specimens. The granite from Shuichang iron mine required to be processed into a cylindrical piece of $\Phi 50 \text{ mm} \times 100 \text{ mm}$ is in good agreement with the sample size recommended by ISRM. The NM-3C nonmetallic ultrasonic tester was used to ensure the uniformity of the physical and mechanical properties of experimental specimens. Through preliminary tests, the uniaxial compressive strength of the granite was determined as 125.71 MPa. The mechanical test equipment and specimens are shown in Figure 1.

2.2. Loading Test Scheme. There are two purposes of loading test: one is to analyze the mechanical characteristics of rock under loading conditions which will be used for comparisons with the subsequent unloading test; the other is to determine the peak stress of the specimen under different confining pressures which will provide the basis for the design of unloading test scheme.

According to the in situ stress measurement results of Shuichang iron mine, the maximum horizontal principal stress is about 25 MPa. Therefore, the triaxial compression tests are controlled by the stress with a constant loading rate of 0.5 MPa/s. The confining pressures are 10 MPa, 15 MPa, 20 MPa, and 25 MPa, respectively.

2.3. Unloading Test Scheme. These unloading schemes are designed to model the stress changing of rock slope due to excavation [18]. Constant axial stress-reducing confining pressure path was selected to carry out unloading tests. Figure 2 shows the designed unloading scheme. First, the axial pressure and confining pressure are increased. Then, the axial stress is increased to 80% of the peak strength. Finally, the axial load is kept as constant, and the confining pressure is gradually reduced until specimen failure. Details about the schemes are as follows.



FIGURE 1: Mechanical test equipment and specimens: (a) uniaxial and triaxial compression testing machine; (b) granite specimens.

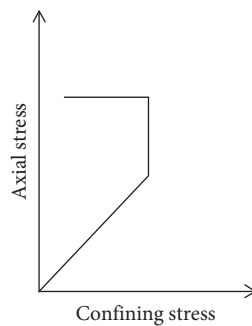


FIGURE 2: Unloading tests scheme: constant axial stress-reducing confining pressure path.

- (1) The stress control with a constant loading rate of 0.1 MPa/s was used to apply confining pressure to predetermined values, which were 10, 15, 20, and 25 MPa, respectively.
- (2) The stress control was continued to apply the axial pressure at the rate of 0.5 MPa/s to the unloading point, where the value of the stress level at unloading point should be greater than uniaxial compressive strength and should be 70–90% of the corresponding triaxial compressive strength. In this study, the starting point of unloading confining pressure was selected as 80% of triaxial compressive strength.
- (3) Keep using stress path control to maintain the axial stress σ_1 . In the same time, the confining pressure was unloaded at the speed of 0.1 MPa/s until the specimen failure.

3. Experimental Results

3.1. Loading Test Results. Figure 3 illustrates the traditional triaxial compression stress-strain curves under different confining pressures. It can be seen from the figure that the curves before the peak basically coincide and have the same trend. As the confining pressure increases, the yield stress, peak stress, and residual strength gradually increase, the radial deformation of the specimen decreases, and the volumetric strain at the peak changes more smoothly,

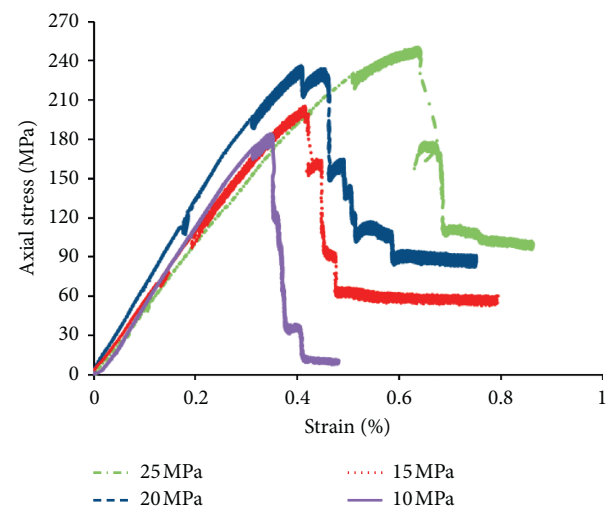


FIGURE 3: Stress-strain curve of the triaxial compression test.

indicating that increasing confining pressure has an inhibiting effect on the deformation and failure of the specimen which improves the load-bearing capacity of the specimen. The postpeak curves show the obvious elastic brittle characteristics and stress drop phenomenon. With the increase of confining pressure, the decrease of stress gradient becomes slower, and the degree of brittle failure after peak decreases.

Figure 4 shows the relationship between the peak strength and confining pressure. The triaxial compressive strength increases with the increase of confining pressure, showing a good linear relationship. Under different confining pressures, the peak strength of the specimens fluctuates with the range of 8.3%, 6.1%, 2.7%, and 4.7%, respectively. Therefore, the results of uniaxial and triaxial compressive strength of the granite have good repeatability.

3.2. Unloading Test Results. Figure 5 shows the full stress-strain curve of unloading at 80% peak strength. It can be seen that the stress-strain curve before the peak is approximately linear during unloading. The increase in the axial strain during the unloading process and after the peak is very small.

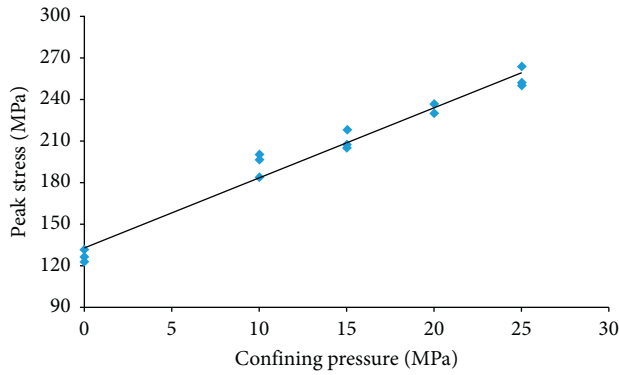


FIGURE 4: Peak strength-confining pressure curve.

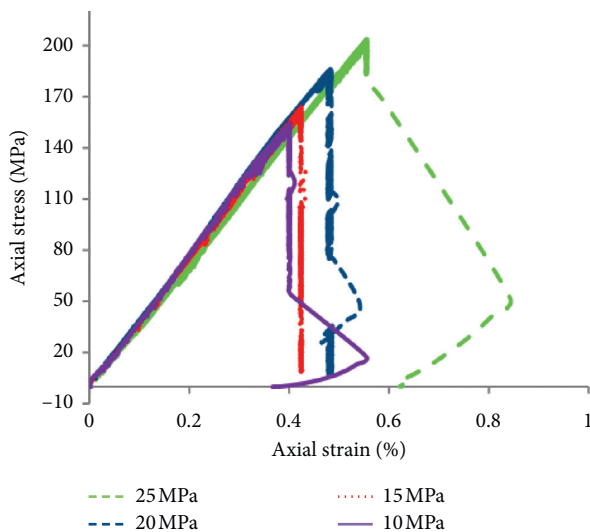


FIGURE 5: Axial stress-strain curves of unloading at 80% peak strength.

The stress drop occurs during the failure, which is sudden and severe, showing strong brittleness.

In the process of unloading confining pressure, the radial strain shows obvious dilatancy and increases rapidly near the failure (Figure 6). With the increase of initial confining pressure, the axial strain increases, while the radial strain and volume strain decrease. This is because that the confining pressure has a certain constraint on the radial deformation, which limits the development of radial deformation, improves the load-bearing capacity of the specimen, and increases the corresponding axial strain. It also shows that the higher the initial confining pressure, the more severe the damage of the specimen.

The relationship between the axial stress and confining pressure is shown in Figure 7. The axial stress, confining pressure, and reduction ratio of confining pressure at failure point under different initial confining pressures are given in Table 1. It can be found that when the confining pressure drops to 66.1% (average proportion) of the initial confining pressure, the axial stress decreases slightly at first. Then, a large stress drop occurs, which results in the failure of the specimen.

Figure 8 shows the radial strain-confining pressure curves. It can be seen that, in the initial stage of unloading confining pressure, the radial strain increases slowly and has a linear relationship with the decrease of confining pressure, indicating that the specimen is in the elastic stage. With the unloading process, the confining pressure decreases, and the radial deformation of the specimen increases rapidly, showing a nonlinear relationship with the confining pressure. Meanwhile, the radial plastic deformation appears, which indicates that the radial deformation is the main reason for the failure of the specimen. The confining pressure has a certain limiting effect on the deformation. Therefore, with the increase of initial confining pressure, the radial strain reduces.

3.3. Comparative Analysis of Loading and Unloading Test Results. Loading and unloading both can lead to the failure of the specimen, but the stress paths of the two tests are completely different. Mohr's circle is used to represent the relationship between stress σ_1 and stress σ_3 in rock mass, as shown in Figure 9.

In the conventional triaxial compression, the axial stress (σ_1) is increased to reach the bearing limit of rock specimen. While in unloading conditions, the confining pressure (σ_3) is reduced and the bearing capacity of rock sample specimen reaches the limit. Whether it is the loading or unloading test, the confining pressure has a great influence on the bearing capacity of the specimens.

Figure 10 shows the comparison of loading and unloading tests under the initial confining pressure of 25 MPa. The stress-strain curve trends of loading and unloading are basically the same in the prepeak stage, and the deviation begins to appear with the unloading process. The axial strain and stress of unloading failure are both smaller than the value of loading test failure. So unloading is more likely to cause rock failure, and the brittle characteristics are more obvious. In the loading test, the damage of the specimen is mainly caused by the axial compression failure. While in the unloading test, there is no obvious plastic characteristic, but the dilatancy characteristic is obvious, indicating that the unloading failure of the specimen is mainly caused by the transverse expansion.

4. Analysis of Micromechanical Properties Based on Numerical Tests

4.1. Construction of the PFC Rock Model. In PFC, the intact rock is represented as assemblage of rigid circular (in 2D) or spherical (in 3D) particles and piece of finite-size interface between two notional surfaces. In this study, the flat joint model (FJM), which can well explain the mechanical behavior of various aspects of rock (i.e., UCS/TS ratio, internal friction angle, and strength envelope), especially the brittle rock, was used to represent the granite. A cylindrical sample model with a cylindrical piece of $\Phi 50 \text{ mm} \times 100 \text{ mm}$, which is in good agreement with the rock sample size recommended by ISRM, is generated to simulate the laboratory test (Figure 11). For obtaining a reliable simulation results, the

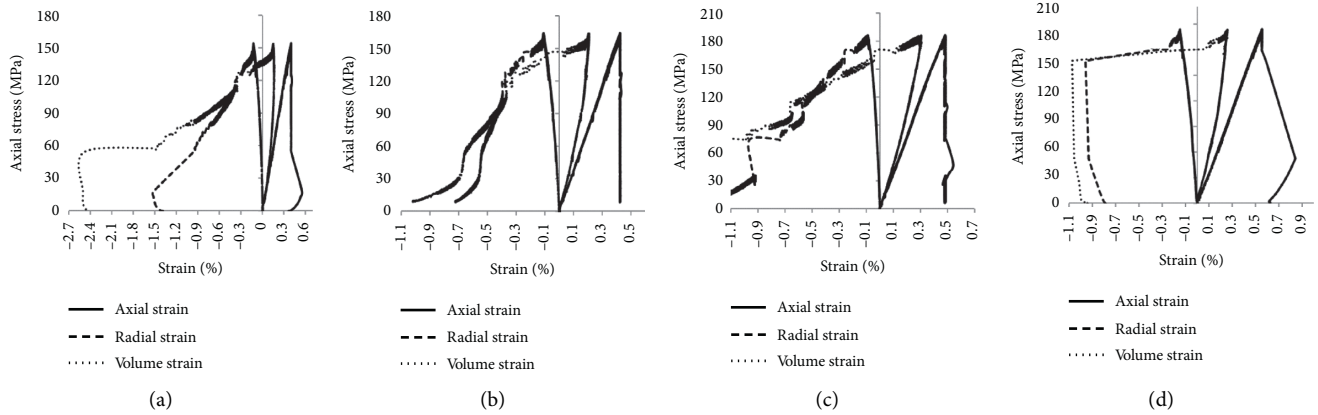


FIGURE 6: Stress-strain curves under different confining pressures: (a) 10 MPa; (b) 15 MPa; (c) 20 MPa; (d) 25 MPa.

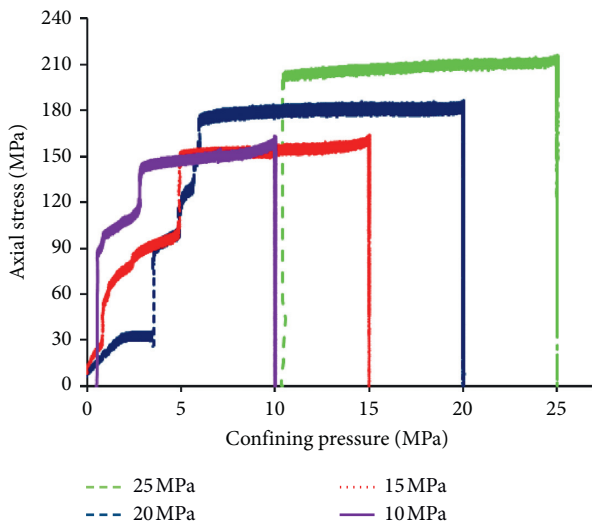


FIGURE 7: Axial stress-confining pressure curve.

ratio of smallest characteristic length for the model to the median particle radius should be 50–100 [38, 46–49]. Considering the computational efficiency and accuracy, the minimum particle radius and particle size ratio are set as 1 mm and 1.66 mm, respectively. So the sample model consisted of 14036 balls with radius varying from 1.00 mm to 1.66 mm.

The “trial-and-error” method is used to determine the microparameters, derived from laboratory tests results, to match the microparameters of the simulation specimen. Primarily, according to the uniaxial compression tests, the deformation properties (i.e., Poisson’s ratio and elastic modulus) of rock specimens are calibrated. Then, the strength properties are matched by triaxial compression tests. The calibration results of the microparameters in PFC are given in Table 2.

Then, the microparameters were verified by using the numerical test. Figure 12 shows the stress-strain curves of the uniaxial compressive test and failure modes from experimental result and numerical result. The stress-strain curves, both before and after the peak, are well consistent with those of the experiment, and the failure patterns from

the experiment and numerical tests are quite similar. Figure 13 shows the stress-strain curve of numerical triaxial loading and unloading tests.

4.2. Acoustic Emission Characteristics. From the microscopic point of view, the instability of materials is caused by the initiation and propagation of microcrack. The contact between particles in PFC is destroyed under the action of shear stress or tensile stress. Every fracture of contact bond is accompanied by a release of energy, which can be regarded as an acoustic emission (AE) event with rock. Therefore, the PFC numerical test can effectively characterize the distribution of shear failure and tensile failure events in the process of loading and unloading tests.

4.2.1. Acoustic Emission Characteristics of the Loading Test.

Figure 14 shows the relationship between stress-strain and the number of microcrack under confining pressure of 20 MPa. As shown in figure, there is a good corresponding relationship between the acoustic emission events and the characteristic stress values of hard brittle rock such as fracture strength and damage strength. At the linear elastic stage, there are few microcracks in the specimen. When the stress increases to about 100 MPa (i.e., 45% of the peak strength), there is a stable microcrack growth in the specimen, with the strength corresponding to the crack initiation strength σ_{CI} . When the stress increases to about 100 MPa (i.e., 78% of the peak strength), there is a rapid microcrack growth in the specimen, and the strength corresponds to the crack damage strength σ_{cd} . When it comes to reach the peak strength, the number of cracks begins to increase significantly, and the macrofailure surface is gradually formed.

In the whole loading process, the tensile cracks account for about 80% of the total cracks. When the load reaches about 85% of the peak strength, the shear cracks begin to initiate, which indicates that the tensile failure is the main failure in the early stage of the test, accompanying by a small amount of shear failure. Under the loading process, the shear cracks increases and reaches the extreme value after the peak. In this stage, the shear failure zone was formed and gradually penetrated into the macrofracture surface, which

TABLE 1: The axial stress, confining pressure, and reduction ratio of confining pressure.

Initial confining pressures (MPa)	Axial stress (MPa)	Confining pressure (MPa)	Reduction ratio (%)
10	145.7	2.98	70.2%
15	154.5	5.02	66.5
20	172.8	6.11	69.45
25	198.8	10.6	57.6

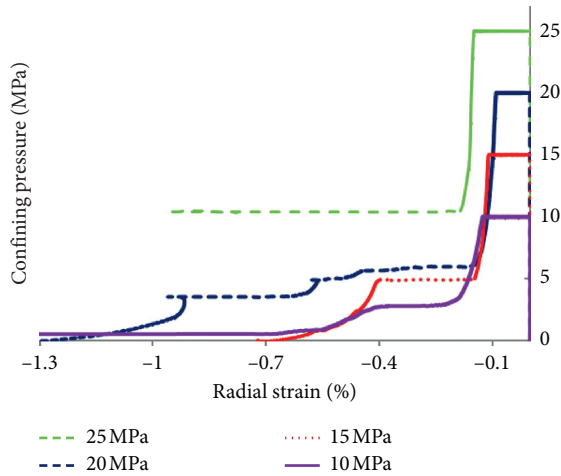


FIGURE 8: Radial strain-confining pressure curve.

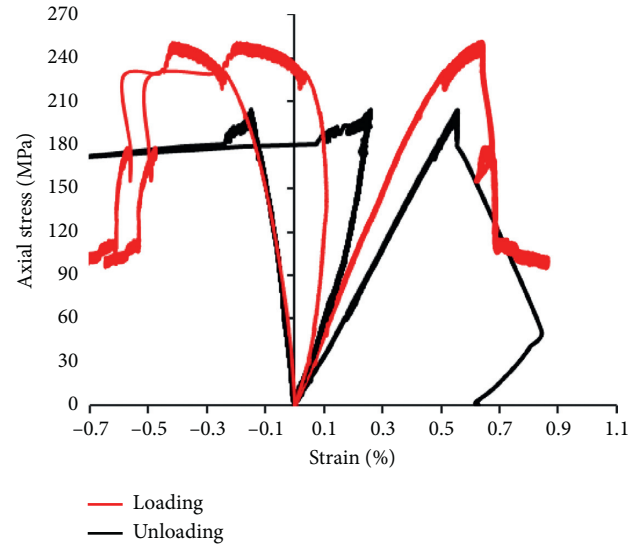


FIGURE 10: Stress-strain curves of different stress paths.

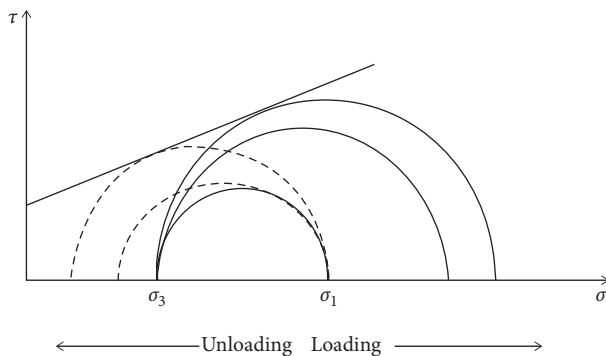


FIGURE 9: Mohr's circle under loading and unloading conditions.

indicated that the shear failure was dominant in the whole failure process, accompanying by tensile failure.

The rosette diagram of microcrack distribution under the confining pressure of 25 MPa is shown in Figure 15. The direction of microcrack is parallel or nearly parallel to axial stress, which is in line with the characteristics of hard brittle rock. It can be seen from Figure 16 that the initiation and propagation trend of microcrack in specimens under different confining pressures are basically the same, and the confining pressure has little effect on them.

4.2.2. *Acoustic Emission Characteristics of the Unloading Test.* Figures 17 and 18 are the rosette diagram and strain-microcrack number curve under the confining pressure of 25 MPa, respectively. It can be seen that the direction of microcrack is mainly parallel or nearly parallel to the axial

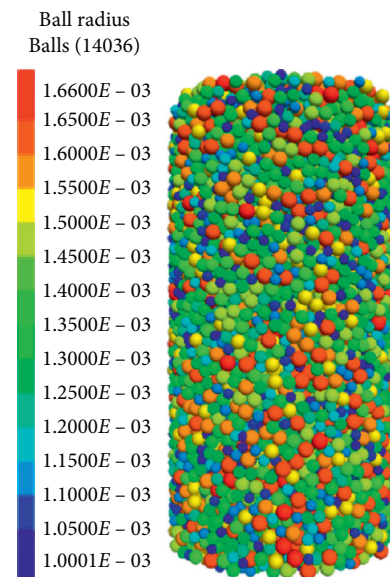


FIGURE 11: PFC numerical model.

stress direction, and the trend is more obvious than that of the loading test. The tensile cracks dominate more than 90% of the total number of cracks, which shows an increase compared to the loading conditions.

The occurrence of tensile cracks under loading conditions is a typical compression-induced tensile cracking phenomenon. Moreover, under unloading conditions causes

TABLE 2: Microparameters of the FJM model after calibration.

Microparameters	Description	Unit	Value
d_{\min}	Minimum particle radius	mm	1.0
d_{\max}/d_{\min}	Particle size ratio	—	1.66
λ	Radius multiplier	—	1
N_r	Number of elements in radial direction	—	1
N_a	Number of elements in circumferential direction	—	3
E_c	Effective modulus of both particle and bond	GPa	76
k_{rat}	Normal-to-shear stiffness ratio of both particle and bond	—	1.8
μ	Friction coefficient	—	0.4
σ_b	Bond tensile strength	MPa	14
c_b	Bond cohesion strength	MPa	135
Φ_b	Friction angle	°	5

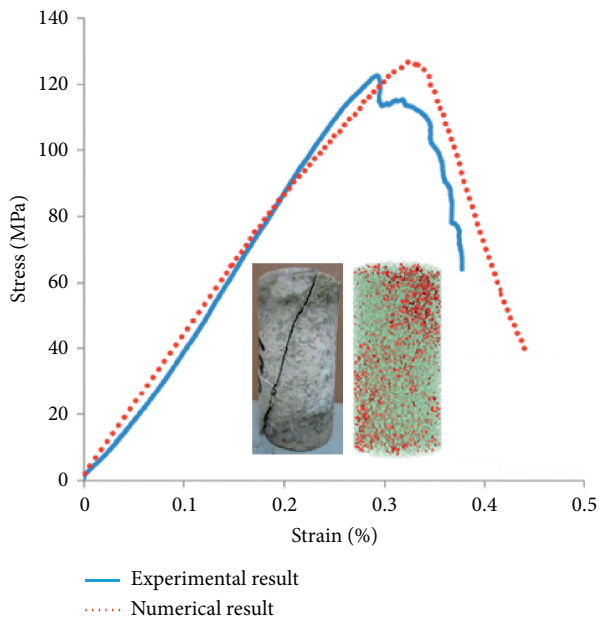


FIGURE 12: Comparison of UCS from experimental and numerical results.

lateral expansion and tensile stresses. Therefore, at the beginning of unloading, the tensile cracks generate fast. The total number of cracks under unloading condition of confining pressure is more than that of the loading condition when the specimen is destroyed. In other words, the unloading failure requires more time and shows a more severe and sudden damage.

4.3. Energy Evolution Law. According to the energy of particles, contact relationship, and bonding relationship between particles, a variety of energy can be recorded in PFC software. The main monitored energy in the FJM model includes five types, E_b (boundary energy, defined as the work performed by the boundary, that is, the total input energy), E_s (strain energy, defined as the linear contact strain energy and bond strain energy), E_μ (dissipation energy, defined as the total energy dissipated by frictional slip and the dashpots), and E_k (kinetic energy, defined as the energy consumed by particle motion).

4.3.1. Energy Evolution Law of the Loading Test. Figure 19(a) shows the energy evolution law of the loading test under confining pressure of 20 MPa. During the test, the upper and lower loading plates and side walls exert pressure on the model, so the boundary energy as the input energy increases all the time. Strain energy corresponds well to the stress-strain curve and reaches the highest value near the peak strength, which is the principal part of microenergy consumption. It reflects the process of the microcrack caused by the breaking of the bond between particles. The strain energy increases gradually and dissipation energy is almost zero before peak strength, while after that, the strain energy reduces sharply and dissipation energy begins to play a dominant role. In this stage, the number of newly formed cracks gradually decreases and the relative sliding between particles increases. Then, the microcrack continuously grows, propagates, and forms macrocrack.

4.3.2. Energy Evolution Law of the Unloading Test. Figure 19(b) shows the energy evolution law of the unloading test under confining pressure of 20 MPa. It can be seen that the energy evolution law under loading and unloading paths is basically similar, but there are obvious differences in magnitude. Before unloading, the trend and quantity of each kind of microenergy are the same as the loading conditions. During the unloading process, the boundary energy and strain energy are less than the energy corresponding to the same strain value under loading condition, while the dissipation energy is on the contrary. For example, when the strain value is 0.005, the boundary energy under loading and unloading conditions is 110.24 N·m and 98.56 N·m, respectively, that is, because the confining pressure begins to do negative work, it leads to the slow growth of boundary energy. The values of strain energy under these two stress paths are 46.13 N·m and 52.74 N·m, respectively. The results show that the number of microcrack under the same strain is more than that under loading condition. Dissipation energy is 11.02 N·m and 6.67 N·m, respectively, which indicates that there is more relative sliding between particles during the unloading process.

4.4. Failure Mode. PFC, as an explicit numerical simulation software, can count the distribution of microcrack in each time step and reveal the progressive failure process of

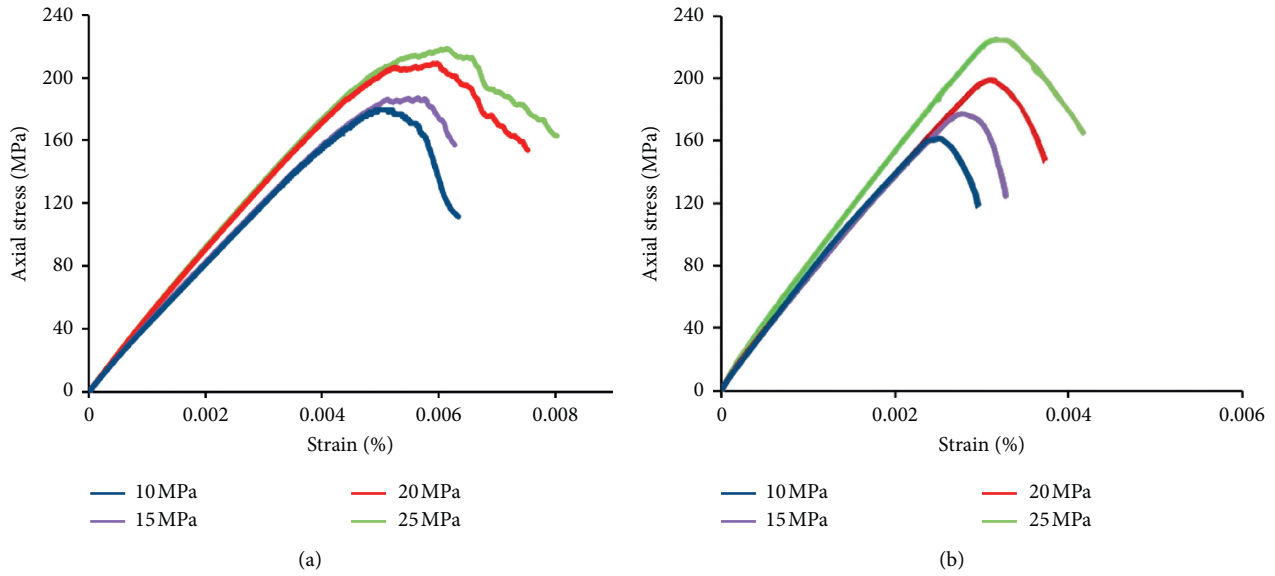


FIGURE 13: Stress-strain curve of numerical triaxial loading and unloading simulations: (a) loading; (b) unloading.

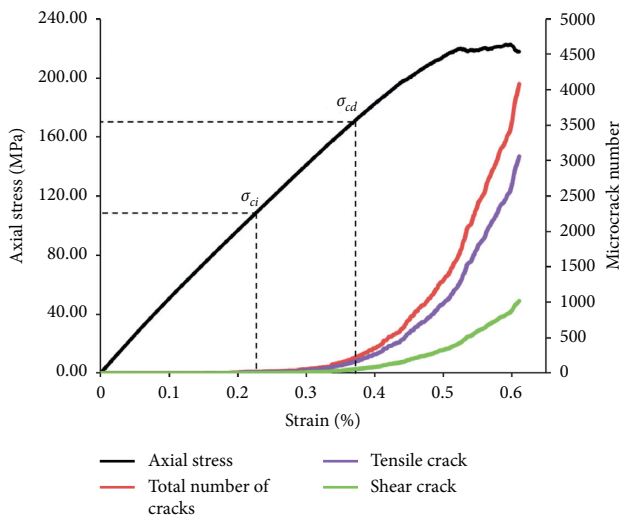


FIGURE 14: Relationship between stress-strain curve and microcrack number.

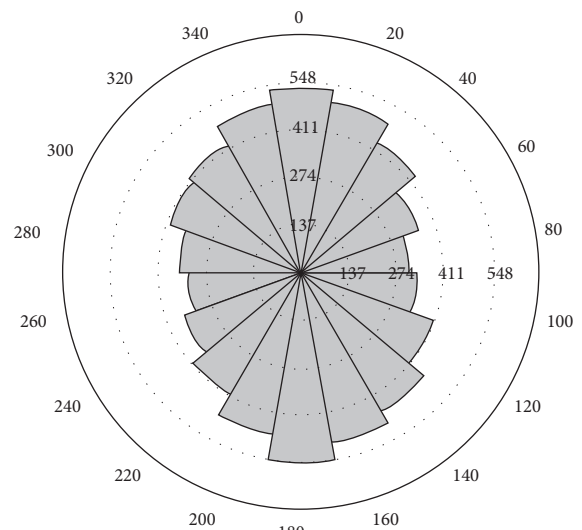


FIGURE 15: The rosette diagram of microcrack distribution.

specimens under loading and unloading conditions by analyzing the initiation, propagation, and penetration of microcrack.

4.4.1. *Failure Mode of the Triaxial Compression Test.* The failure of granite under loading is mainly controlled by shear crack. Figure 20 shows the whole process of shear crack from generation and development to penetration under the confining pressure of 15 MPa.

At 80% of the peak strength, since it has just entered the plastic stage, there are few shear cracks, which are mainly distributed at the top and around the specimen. This is mainly caused by the end effect. Along with the loading process, the shear cracks gradually increase from the two ends of the specimen to the middle part. At 90% of the peak

strength, the shear failure of the two ends is glaringly obvious, and the middle part has a tendency of penetration. The microcrack grows faster near the peak, mainly concentrated in the middle part. When the specimen is damaged, the crack ruptures and forms a main failure surface, which is a certain angle of inclined plane shear failure. In addition, due to the end effect at both ends of the specimen, the density of shear cracks is relatively high, and secondary failure surfaces are formed on the top of the specimen.

4.4.2. *Failure Mode of the Unloading Test.* Figure 21 shows the whole process of microcrack from germination, development to penetration in the 25 MPa unloading confining pressure test. The development law of microcrack is basically the same as the loading process. The stress at the unloading

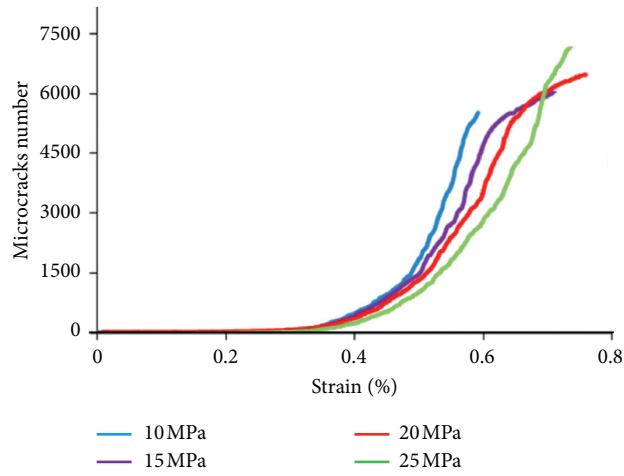


FIGURE 16: Strain-microcrack number curve.

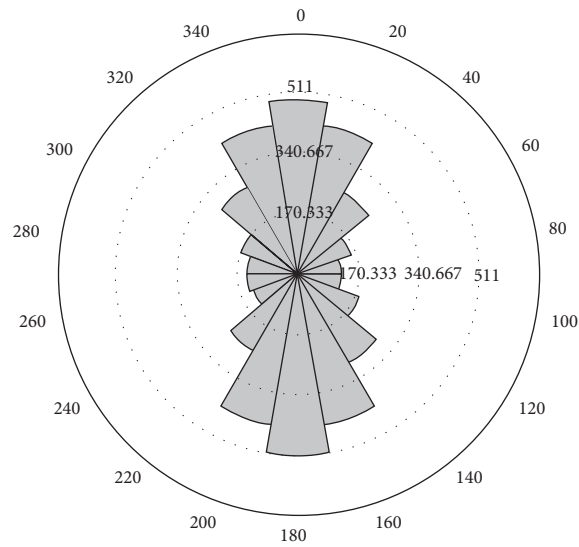


FIGURE 17: The rosette diagram of microcrack distribution.

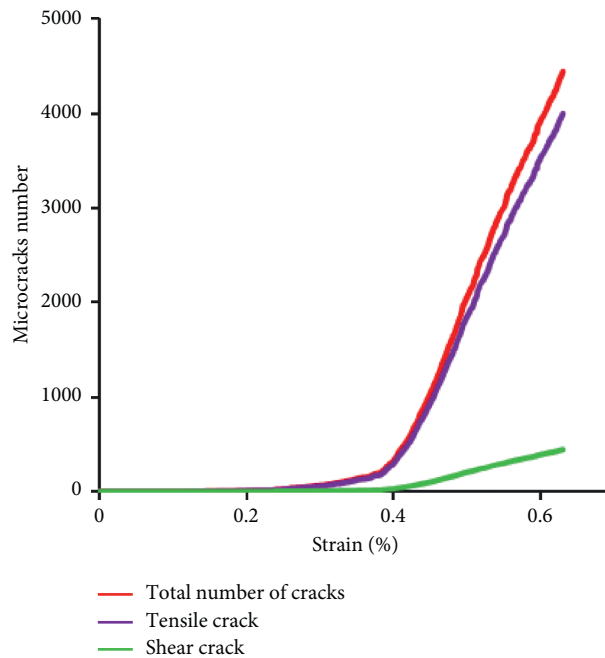


FIGURE 18: Strain-microcrack number curve.

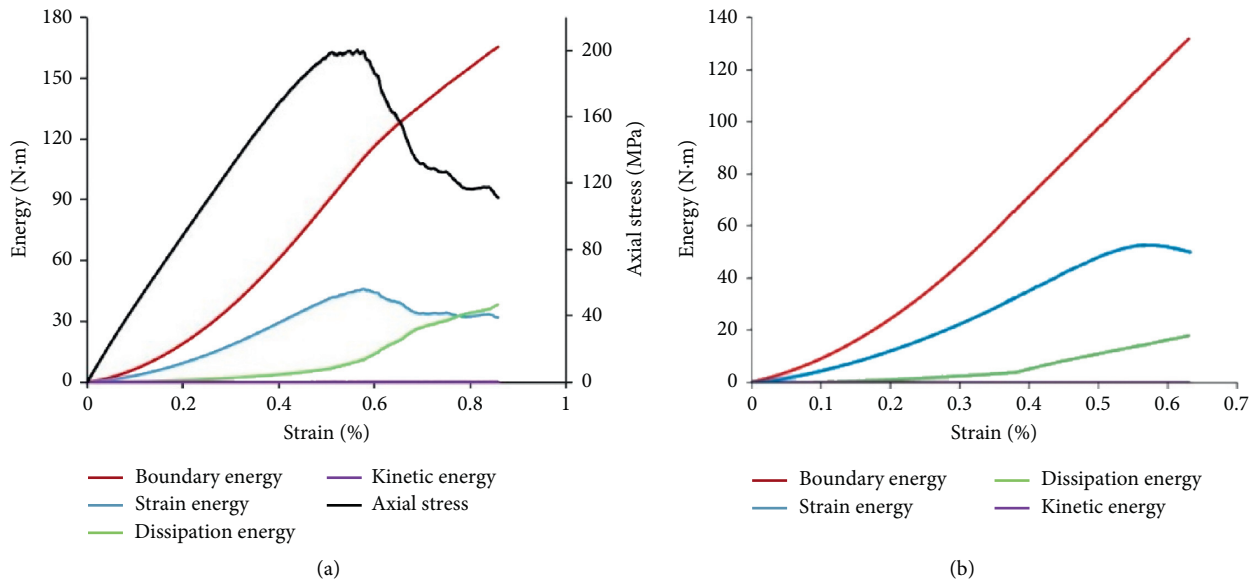


FIGURE 19: Energy and stress curves of rock deformation: (a) loading; (b) unloading.

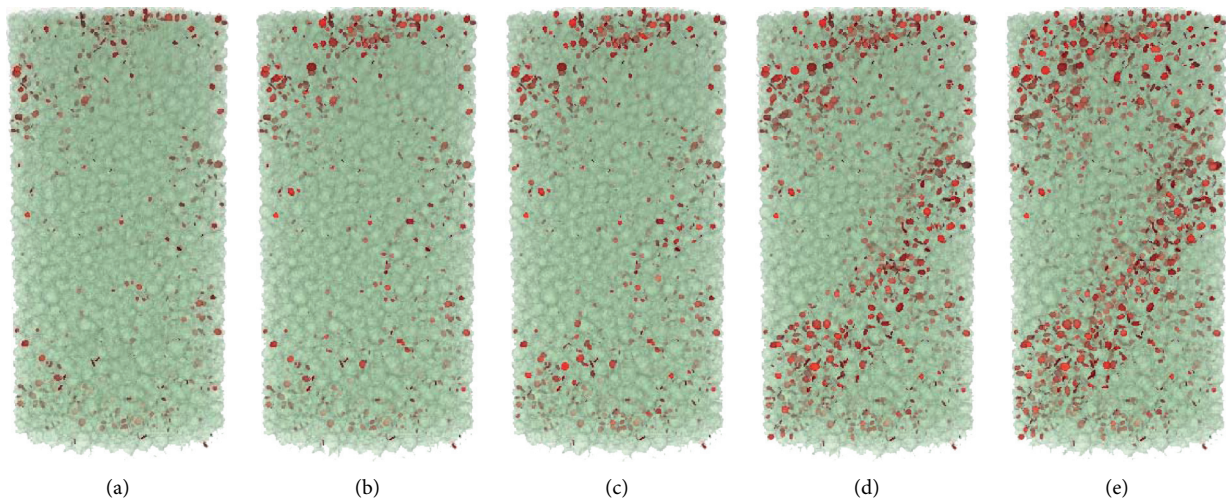


FIGURE 20: Microcrack growth process in the triaxial compression test: (a) prepeak (80%); (b) prepeak (85%); (c) prepeak (90%); (d) peak stress; (e) postpeak (20%).

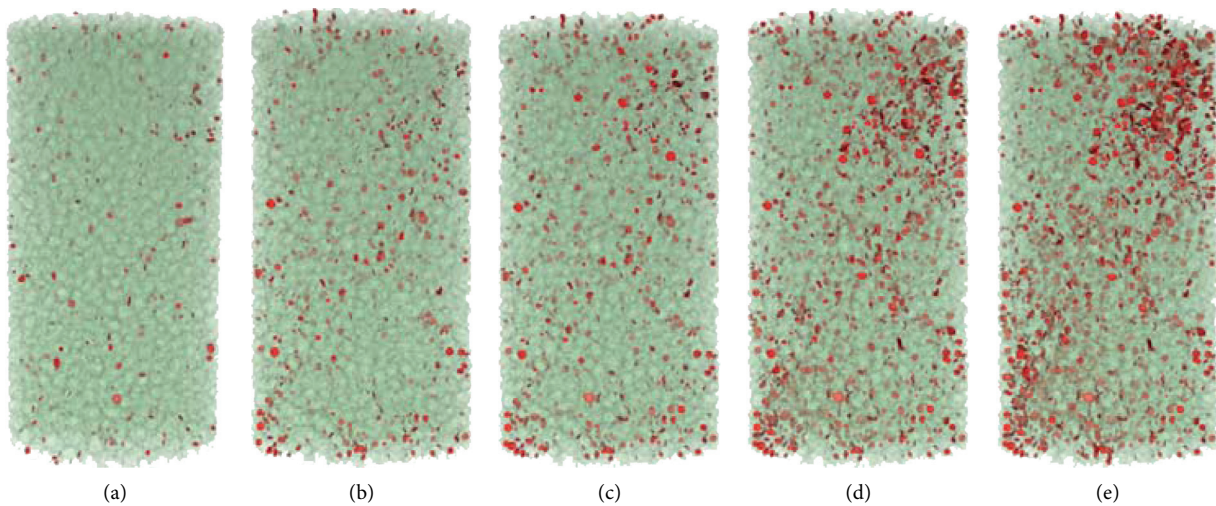


FIGURE 21: Microcrack growth process in the unloading test: (a) prepeak (80%); (b) prepeak (85%); (c) prepeak (90%); (d) peak stress; (e) postpeak (20%).

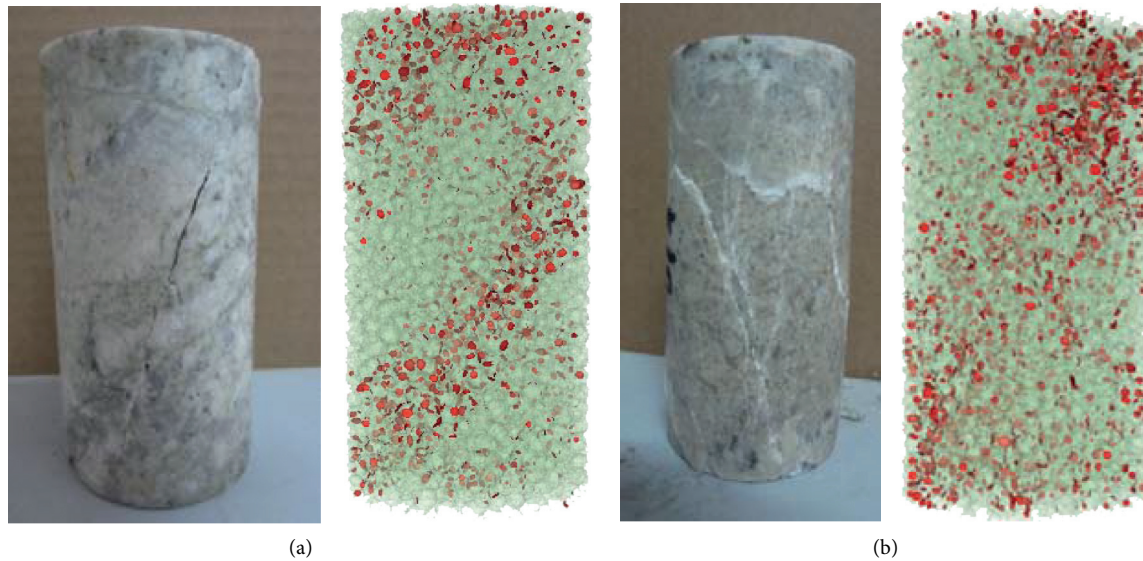


FIGURE 22: Comparison of failure modes from experimental and numerical tests: (a) loading test; (b) unloading test.

point of the confining pressure set in this study is 80% of the peak strength, so the 80% stage before the peak is the triaxial loading stage. At 85% before the peak, that is, after the unloading of the confining pressure begins, the number of microcrack begins to increase, and the distribution is relatively discrete. Compared with the loading test, the number of cracks before the peak increases sharply with a fast growth rate of microcrack and large number of cracks. The failure mode of postpeak specimens is more complicated than that of loading. Besides a main failure surface, there are also multiple shear zones parallel to or intersecting with the main failure surface. In addition, there are local shear failure surfaces at the top and bottom.

Figure 22 is a comparison of failure modes from experimental and numerical tests. The macroscopic fracture surface distribution of the specimen is similar to the numerical simulation results, which also verifies the reliability of the numerical test results.

5. Conclusion

In this study, the conventional triaxial compression test, unloading test, and numerical simulations were carried out on Shuichang iron mine granite. The stress-strain curves and the number of microcrack under different stress paths were obtained. Based on those results, the mechanical properties and failure law of granite under loading and unloading conditions were investigated from macro-micro viewpoint. The conclusions of this study are as follows:

- (1) Under loading conditions, granite specimen shows obvious elastic-brittle characteristics. With the increase of confining pressure, the postpeak stress drops faster and faster. Moreover, under unloading conditions, the brittle failure of specimens is more obvious. For the loading or unloading test, the confining pressure has a great impact on the bearing capacity of the specimen. The higher the initial

confining pressure, the higher the bearing capacity of the specimen is.

- (2) Both loading and unloading stress paths can damage rock specimens. But the two stress paths to failure are completely different, and the unloading path is more likely to cause rock severe damage. Experimental results show that when the confining pressure drops to 66.1% of the initial confining pressure, the specimen loses its load-bearing capacity and destroyed, due to the lateral expansion.
- (3) Numerical experiments show that the directions of microcrack in the specimens are mainly parallel or approximately parallel to the axial stress direction, and most of the cracks are tensile cracks. Under the unloading condition, the crack initiation speed is faster, and almost all of them are tensile cracks. The unloading damage is characterized by the short-time, severe degree, and paroxysm.
- (4) The failure of granite under loading is mainly controlled by shear cracks. When the specimen is damaged, an inclined plane is formed as the main failure surface. Under unloading conditions, the development speed of microcrack is faster and more tensile cracks are generated. The failure mode of the specimen under unloading is more complicated than that under loading. Besides the main failure surface, there are also many shear zones parallel to or intersecting with the main failure surface.

Data Availability

The data used to support the findings of this study are available from the corresponding author upon request.

Conflicts of Interest

The authors declare that there are no conflicts of interest.

Acknowledgments

This research was funded by the National Natural Science Foundation of China (51034001).

References

- [1] J. A. Hudson and J. P. Harrison, *Engineering Rock Mechanics: An Introduction to the Principles*, Elsevier, Oxford, UK, 2000.
- [2] W. Gang, "Comparative analysis of failure effects under unloading conditions," *Rock and Soil Mechanics*, vol. 2, pp. 13–16, 1997.
- [3] J.-L. Li and L. H. Wang, *Theories of Unloading Rock Mass Mechanics and its Engineering Practice*, Science Press, Beijing, China, 2016.
- [4] J.-L. Li, *Unloading Rock Mass Mechanics*, China Water & Power Press, Beijing, China, 2003.
- [5] E. Z. Lajtai, "A mechanistic view of some aspects of jointing in rocks," *Tectonophysics*, vol. 38, no. 3-4, pp. 327–338, 1977.
- [6] J. S. O. Lau and N. A. Chandler, "Innovative laboratory testing," *International Journal of Rock Mechanics and Mining Sciences*, vol. 41, no. 8, pp. 1427–1445, 2004.
- [7] F. Trippetta, C. Colletini, P. G. Meredith, and S. Vinciguerra, "Evolution of the elastic moduli of seismogenic Triassic Evaporites subjected to cyclic stressing," *Tectonophysics*, vol. 592, pp. 67–79, 2013.
- [8] N. A. Chandler, "Quantifying long-term strength and rock damage properties from plots of shear strain versus volume strain," *International Journal of Rock Mechanics and Mining Sciences*, vol. 59, pp. 105–110, 2013.
- [9] J.-H. Shen, L.-S. Wang, Q.-H. Wang et al., "Deformation and fracture features of unloaded rock mass," *Chinese Journal of Rock Mechanics and Engineering*, vol. 22, pp. 2028–2031, 2003.
- [10] X. Xi, S. Yang, C. I. McDermott, and Z. Shipton, "Modelling rock fracture induced by hydraulic pulses," *Rock Mechanics and Rock Engineering*, pp. 1–18, 2021.
- [11] X.-G. Zhao, J. Wang, M. Cai et al., "Influence of unloading rate on the strain burst characteristics of beishan granite under true-triaxial unloading conditions," *Rock Mechanics and Rock Engineering*, vol. 20, no. 5, pp. 472–480, 2014.
- [12] M.-J. Zhao, "Study on a constitutive model of rock under triaxial loading and unloading," *Chinese Journal of Rock Mechanics and Engineering*, vol. 21, no. 5, pp. 626–631, 2002.
- [13] W.-U. Gang, J. Sun, and Z.-R. Wu, "Damage mechanical analysis of unloading failure of intact rock under complex stress state," *Journal of Hohai University*, vol. 25, no. 3, pp. 44–48, 1997.
- [14] A. M. Al-Ajmi and R. W. Zimmerman, "Relation between the Mogi and the coulomb failure criteria," *International Journal of Rock Mechanics and Mining Sciences*, vol. 42, no. 3, pp. 431–439, 2005.
- [15] D.-Y. Li, T. Xie, X.-B. Li et al., "On the Mogi-Coulomb strength criterion as applied to rock triaxial unloading test," *Science and Technology Review*, vol. 33, no. 9, pp. 84–91, 2015.
- [16] D.-Y. Li, Z. Sun, X.-B. Li, and T. Xie, "Mechanical response and failure characteristics of granite under different stress paths in triaxial loading and unloading conditions," *Chinese Journal of Rock Mechanics and Engineering*, vol. 35, no. S2, pp. 3449–3458, 2016.
- [17] Y.-H. Lv, Q.-H. Liu, and Y.-H. Hu, "Damage deformation characteristics and its strength criterion based on unloading experiments of granites," *Chinese Journal of Rock Mechanics and Engineering*, vol. 28, no. 10, pp. 2096–2103, 2009.
- [18] R. Q. Huang, X. N. Wang, and L. S. Chan, "Triaxial unloading test of rocks and its implication for rock burst," *Bulletin of Engineering Geology and the Environment*, vol. 60, no. 1, pp. 37–41, 2001.
- [19] R.-Q. Huang and D. Huang, "Experimental research on mechanical properties of granites under unloading condition," *Chinese Journal of Rock Mechanics and Engineering*, vol. 27, no. 11, pp. 2205–2213, 2008.
- [20] Y. Fang, W.-B. Lu, and Y.-H. Zhou, "Study on energy release process of high energy storage rock mass induced by excavation unloading," *Chinese Journal of Rock Mechanics and Engineering*, vol. 35, no. 2, pp. 3706–3715, 2016.
- [21] S.-L. Qiu, X.-T. Feng, C.-Q. Zhang, and H. Zhou, "Experimental research on mechanical properties of deep-buried marble under different unloading rates of confining pressures," *Chinese Journal of Rock Mechanics and Engineering*, vol. 31, no. 8, pp. 1686–1697, 2012.
- [22] K.-P. Zhou, S.-H. Su, Z.-X. Hu, and Z. Yang, "Experimental research into nuclear magnetic resonance in marble with different initial damages under unloading conditions," *Rock and Soil Mechanics*, vol. 36, no. 8, pp. 2144–2150, 2015.
- [23] X.-R. Liu, J. Liu, D.-L. Li, and C. He, "Experimental research on the effect of different initial unloading levels on mechanical properties of deep-buried sandstone," *Rock and Soil Mechanics*, vol. 38, no. 11, pp. 3081–3088, 2017.
- [24] Z.-X. Hu, K.-P. Zhou, J.-L. Li, and F. Gao, "Meso-damage evolution of unloading rock mass based on nuclear magnetic resonance technology," *Journal of University of Science and Technology Beijing*, vol. 36, no. 12, pp. 1567–1574, 2014.
- [25] J.-X. Ren and X.-R. Ge, "Real-time computerized tomography(CT) test of failure process of jointed granite under unloading in three gorges project(TGP)," *Journal of Coal Science and Engineering*, vol. 10, no. 2, pp. 11–14, 2004.
- [26] Z.-Q. Yang, S.-H. Wang, Y.-R. Meng et al., "The 3D numerical specimen of granite based on CT technology and application," *Chinese Journal of Solid Mechanics*, vol. 38, no. 6, pp. 591–600, 2017.
- [27] N. Erarslan and D. J. Williams, "The damage mechanism of rock fatigue and its relationship to the fracture toughness of rocks," *International Journal of Rock Mechanics and Mining Sciences*, vol. 56, pp. 15–26, 2012.
- [28] X. Xi, X. Wu, Q. Guo, and M. Cai, "Experimental investigation and numerical simulation on the crack initiation and propagation of rock with pre-existing cracks," *IEEE Access*, vol. 8, pp. 129636–129644, 2020.
- [29] P. A. Cundall and O. D. L. Strack, "Discussion: a discrete numerical model for granular assemblies," *Géotechnique*, vol. 30, no. 3, pp. 331–336, 1980.
- [30] Itasca Consulting Group Inc, *PFC (Version 5.0) Manual*, Itasca Consulting Group Inc, Minneapolis, MN, USA, 2014.
- [31] D. O. Potyondy and P. A. Cundall, "A bonded-particle model for rock," *International Journal of Rock Mechanics and Mining Sciences*, vol. 41, no. 8, pp. 1329–1364, 2004.
- [32] M. Cai, P. Kaiser, Y. Tasaka, and M. Minami, "Peak and residual strengths of jointed rock masses and their determination for engineering design," *Rock Mechanics: Meeting Society's Challenges and Demands*, pp. 259–267, 2007.
- [33] M. Cai, P. K. Kaiser, and C. D. Martin, "Quantification of rock mass damage in underground excavations from microseismic event monitoring," *International Journal of Rock Mechanics and Mining Sciences*, vol. 38, no. 8, pp. 1135–1145, 2001.
- [34] B. An and D. D. Tannant, "Discrete element method contact model for dynamic simulation of inelastic rock impact," *Computers & Geosciences*, vol. 33, no. 4, pp. 513–521, 2007.

- [35] Y. Zhou, A. Misra, and S.-C. Wu, "Macro- and meso-analyses of rock joint direct shear test using particle flow theory," *Chinese Journal of Rock Mechanics and Engineering*, vol. 31, no. 6, pp. 1245–1256, 2012.
- [36] Y. Zhou, S.-C. Wu, Y.-T. Gao, and A. Misra, "Macro and meso analysis of jointed rock mass triaxial compression test by using equivalent rock mass (ERM) technique," *Journal of Central South University*, vol. 21, no. 3, pp. 1125–1135, 2014.
- [37] Y. Zhou, G. Han, and S.-C. Wu, "Meso failure mechanism of rock mass and slope with intermittent joints," *Chinese Journal of Rock Mechanics and Engineering*, vol. 35, no. 2, pp. 3878–3889, 2016.
- [38] D. Mas Ivars, M. E. Pierce, C. Darcel et al., "The synthetic rock mass approach for jointed rock mass modelling," *International Journal of Rock Mechanics and Mining Sciences*, vol. 48, no. 2, pp. 219–244, 2011.
- [39] J. A. Vallejos, K. Suzuki, A. Brzovic, and D. M. Ivars, "Application of Synthetic Rock Mass modeling to veined core-size samples," *International Journal of Rock Mechanics and Mining Sciences*, vol. 81, pp. 47–61, 2016.
- [40] Y. Cong, Y. Cong, L.-M. Zhang et al., "3D particle flow simulation of loading-unloading failure process of marble," *Rock and Soil Mechanics*, vol. 40, no. 3, pp. 1179–1186, 2019.
- [41] Z. Guo, Q. Wang, S. Yin et al., "The creep compaction behavior of crushed mudstones under the step loading in underground mining," *International Journal of Coal Science & Technology*, vol. 6, no. 3, pp. 408–418, 2019.
- [42] W. Pan, X. Wang, Q. Liu, Y. Yuan, and B. Zuo, "Non-parallel double-crack propagation in rock-like materials under uniaxial compression," *International Journal of Coal Science & Technology*, vol. 6, no. 3, pp. 372–387, 2019.
- [43] C. Peng, Q. Guo, Z. Yan, M. Wang, and J. Pan, "Investigating the failure mechanism of jointed rock slopes based on discrete element method," *Advances in Civil Engineering*, vol. 2020, pp. 1–19, 2020.
- [44] A. Busaidi, J. F. Hazzard, and R. P. Young, "Distinct element modeling of lac du bonnet granite," *Journal of Geophysical Research*, vol. 110, no. 6, pp. 23–31, 2005.
- [45] H. Yu, H.-S. Jia, S.-W. Liu, and Z. Liu, "Macro and micro grouting process and the influence mechanism of cracks in soft coal seam," *International Journal of Coal Science and Technology*, 2021.
- [46] M. Pierce, P. Cundall, D. Potyondy, and D. Ivars, "A synthetic rock mass model for jointed rock," *Rock Mechanics: Meeting Society's Challenges and Demands*, in *Proceedings of the 1st Canada-US Rock Mechanics Symposium-Rock Mechanics Meeting Society's Challenges and Demands*, pp. 341–349, Vancouver, Canada, June 2007.
- [47] X.-T. Yin, Y.-N. Zheng, and S.-K. Ma, "Study of inner scale ratio of rock and soil material based on numerical tests of particle flow code," *Rock and Soil Mechanics*, vol. 32, no. 4, pp. 1211–1215, 2011, in Chinese.
- [48] X.-B. Ding, L.-Y. Zhang, H.-H. Zhu, and Q. Zhang, "Effect of model scale and particle size distribution on pfc3d simulation results," *Rock Mechanics and Rock Engineering*, vol. 47, no. 6, pp. 1–18, 2013.
- [49] S. Wu and X. Xu, "A study of three intrinsic problems of the classic discrete element method using flat-joint model," *Rock Mechanics and Rock Engineering*, vol. 49, no. 5, pp. 1813–1830, 2016.